

A Three-Dimensional Analysis of Magnetic Nanopattern Formation in FeRh Thin Films on MgO Substrates: Implications for Spintronic Devices

Dániel Géza Merkel,* Gergő Hegedűs, Maria Gracheva, András Deák, Levente Illés, Attila Németh, Fernando Maccari, Iliya Radulov, Márton Major, Aleksandr I. Chumakov, Dimitrios Bessas, Dénes Lajos Nagy, Zsolt Zolnai, Sára Graning, Klára Sájerman, Edit Szilágyi, and Attila Lengyel



Cite This: *ACS Appl. Nano Mater.* 2022, 5, 5516–5526



Read Online

ACCESS |

Metrics & More

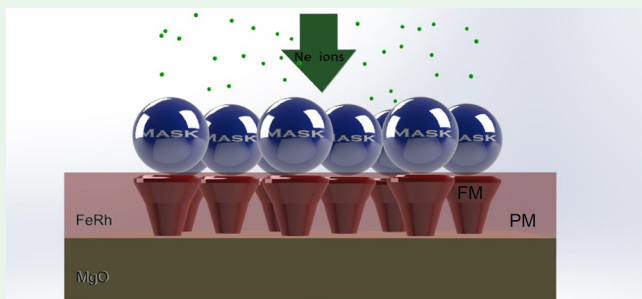
Article Recommendations



Supporting Information

ABSTRACT: Magnetic nanopatterns were successfully created in FeRh thin film deposited on MgO (100) substrates. Silica and polystyrene spherical masks, nominally 500 and 1000 nm in diameter, respectively were applied on the surface of the sample in order to locally shadow the film against the effect of 110 keV energy neon-ion irradiation with fluences of 10^{15} and 10^{16} ions/cm². Such nanosphere-lithography technique allows for projecting the mask geometry on the magnetic structure of the FeRh film. Conversion-electron Mössbauer spectroscopy and magnetic force microscopy were used to determine the ferromagnetic ratio and the magnetic pattern in the samples, and nuclear resonance scattering of synchrotron radiation was applied to obtain the in-depth magnetic profile. From the results obtained, the possible three-dimensional (3D) structure of the created individual magnetic domains was also constructed. Overall, the great customizability of the presented nanosphere-lithography technique in FeRh thin film provides opportunities for developing cutting-edge spintronic applications.

KEYWORDS: thin films, magnetic nanostructures, ion-beam lithography, FeRh, spintronics



INTRODUCTION

The equiatomic alloy of Fe and Rh has been the subject of several studies because of its great diversity of phases of different magnetic behavior.¹ As a result, it has great potential to be used in a large variety of fields such as information technology and energy-saving applications.^{2–9} Also, it is a nontoxic biocompatible material, which exhibits a giant inverse magnetocaloric effect (MCE) near room temperature. Its caloric parameters $\Delta S \sim 20 \text{ J K}^{-1} \text{ kg}^{-1}$ and $\Delta T \sim 13 \text{ K}$ (in 2 T magnetic field)^{10–12} make this alloy a highly competitive candidate for hazardous-gas-free domestic magnetic refrigerators, medical implants, or for a new medical application in cancer treatment.^{13–17}

By increasing the temperature, the FeRh alloy undergoes a metamagnetic transition from the low-temperature antiferromagnetic (AFM) phase to the high-temperature ferromagnetic (FM) phase.^{18–24} In the AFM phase, the magnetic moment of the Fe atoms is $3.3 \mu\text{B}$ of opposite directions, while the magnetic moment of the Rh atoms is insignificant. In the FM phase, Fe and Rh atoms possess parallel moments of 3.2 and $0.9 \mu\text{B}$, respectively.^{25–27} This transition is reversible and numerous studies have been conducted using various methods, such as introducing strain or triggering the magnetic

transformation by deformation.²⁸ An alternative way of manipulating the phase transition is applying strain through piezoelectricity either by introducing an external electric field to the sample,^{18,29} by applying different (W, V, MgO) buffer layers,^{30–32} or by varying the substrate temperature during or after the film deposition.³³

Because of the considerable impact of the FM bcc B2 \leftrightarrow paramagnetic (PM) fcc A1 phase transition of the FeRh system on the magnetic properties, it has been the subject of intensive investigations. The respective B2 \rightarrow A1 and the A1 \rightarrow B2 transitions were induced either by annealing the bulk FeRh alloy, followed by a quenching procedure or by plastic deformation in ball milling and by annealing.^{34,35}

Recently, several studies have been published on tailoring the magnetic and structural properties of FeRh by ion irradiation. A wide variety of ions and energies such as 30

Received: February 2, 2022

Accepted: March 7, 2022

Published: March 17, 2022



keV Ga⁺³⁶, 1 MeV proton,³⁷ 20 keV Ne⁺,³⁸ 120 keV Ne⁺,³⁹ 10 MeV I⁺,^{37,40} 50 keV Ar⁺,⁴¹ 5 keV N⁺,⁴² or 3.8 keV He⁺⁴³ were applied to manipulate the FM–AFM, FM–PM transition, as well as to induce the B2 → A1 structural transformation. By the manipulation of magnetic phases using 25 keV Ne⁺ irradiation, simultaneous coexistence of three magnetic phases (FM, PM, and AFM) was demonstrated.⁴⁴ Jiang et al. investigated the electrical control of phase transition via the combination of ionic liquid and oxide gating.⁴⁵

A key requirement for novel magnetic applications is building a system with laterally alterable magnetic properties.^{46–48} Our group successfully demonstrated in FePd thin film that masked irradiation is an effective tool to create magnetic nanopattern by selectively triggering the L1₀ → A1 structural transition.⁴⁹ Krupinski and co-workers used a similar technique for nanopatterning in Fe₆₀Al₄₀ system by means of the B2 → A2 transition.⁵⁰ In the same system, Ehrler et al. used ~100 fs laser pulses to reversibly switch FM ordering on and off by exploiting a chemical order–disorder phase transition,⁵¹ Polushkin et al. applied high-intensity laser irradiation for (re)writing the ferromagnetism observed at room temperature,⁵² and Graus et al. demonstrated the formation of periodic magnetic nanostructures by direct laser interference patterning.⁵³ Recently, Cress and co-workers reported that by using focused He⁺ irradiation, the metamagnetic transition temperature of the B2 phase could be locally modified in FeRh, leading to FM–AFM lateral magnetic nanostructures,⁴ while Foerster et al. proved the possibility to locally modify the AFM–FM transition temperature in FeRh films by means of nanoindentation.⁵⁴ Compared to the impressive studies of the research groups in the field, our study focuses on the B2–A1 phase transition, which was not demonstrated in the FeRh system in a nanometer scale up to now.

In the present research, we successfully prepared FM domains in the PM matrix by covering the FM layer with spherical masks and destroying ferromagnetism in between masks with ion beam. As a further step, the three-dimensional (3D) shape of the formed FM regions was also determined. It became possible because of nuclear resonance scattering experiments carried out at different scattering angles, which provided the in-depth characterization of the magnetic domains. Combined with lateral mapping, a 3D view similar to that recorded in tomographic patterns has become accessible for the domain structure under the model assumption that the magnetic domains have a cylindrical symmetry. This is, in today's setting, something essential when it comes to the apparent rise of nanodevices. For a comprehensive characterization, we applied grazing-incidence nuclear resonance scattering (GINRS), conversion-electron Mössbauer spectroscopy (CEMS), and magnetic force microscopy (MFM). Here, we show that the lateral and in-depth magnetic profiles resulting from the experiments make possible the 3D analysis of the magnetic domains for each type of mask geometry and irradiation fluence. Our concept opens the way to 3D tailoring the shape of magnetic regions embedded in a PM matrix.

EXPERIMENTAL METHODS

The [^{nat}Fe₅₁Rh₄₉(63 Å)/⁵⁷Fe₅₁Rh₄₉(46 Å)]₁₀ isotope-periodic multilayer (Figure 1) was prepared on a MgO(100) substrate using the molecular beam epitaxy (MBE) technique. From the point of view of chemical and structural properties, the film can be treated as a

Layer structure of the sample

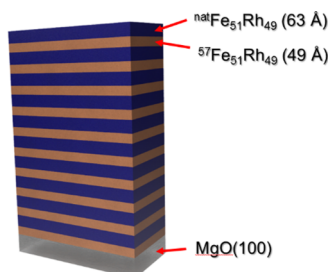


Figure 1. Scheme of the layer structure FeRh thin film.

homogeneous layer, having the advantage of isotope periodicity being utilized in another study. The applied preparation parameters and detailed characterization of the as-deposited sample were reported in a previous study.³⁹ In order to achieve a fully FM B2 structure, the as-deposited sample was annealed at 500 °C for 40 min under high-vacuum conditions of about 10⁻⁷ mbar.

As irradiation masks, a single monolayer of silica or polystyrene spheres of nominally 500 or 1000 nm diameter, respectively, were deposited on the surface of the initially completely FM sample, using the Langmuir–Blodgett technique (KSV 2000).⁵⁵ The silica nanoparticles were prepared by the controlled hydrolysis of tetraethyl orthosilicate (Stöber's method),⁵⁶ while the polystyrene particles were obtained from Microparticles GmbH. After the Langmuir–Blodgett monolayer spheres were prepared on the FeRh film, field emission scanning electron microscopy (FESEM) images were recorded on each sample (Figure 2) using a Zeiss LEO 1540 XB microscope operated at 5 keV acceleration voltage.

The FESEM images were evaluated by the Gwyddion software.⁵⁷ From the analysis of the size distribution of spherical mask layers, the respective mean values of 485.4 nm diameter with a full width at half maximum (FWHM) of 22.2 and 822.6 nm diameter with an FWHM of 22.2 nm for the silica and polystyrene spheres were obtained. The surface coverages were found to be 58(9) and 73(7)% for the silica and the polystyrene spheres, respectively. Throughout the study, the numbers in parentheses mean the standard deviation in the least significant digits. Considering the theoretical close packing of monodisperse spheres, the maximum coverage is approximately 0.907 based on the area ratio of a circle and the enclosing hexagon. This theoretical limit, however, cannot be expected in practice for several reasons. First, there is small, but not negligible size variation of the particles. Second, these particles always form domains at the water/air interface during the film preparation, further reducing the coverage. Additionally, as we used vertical film transfer for the LB film preparation and the films are only weakly cohesive, the observed variations in the coverage are natural for such films.

Two samples covered by silica mask and another two masked by polystyrene spheres were irradiated by 110 keV Ne⁺ ions with two different fluences of 10¹⁵ and 10¹⁶ ion/cm². The irradiation was carried out at the Wigner Research Centre for Physics using the 450 kV heavy-ion cascade implanter. In order to achieve laterally homogenous irradiation, the ~1 mm wide ion beam with a current density of 750 nA/cm² was scanned across the sample surface in both lateral directions. Throughout the entire process, the samples were kept under a vacuum of about 3 × 10⁻⁷ mbar. Based on the detailed full-cascade Monte-Carlo simulation using the SRIM code,⁵⁸ the energy of the Ne⁺ ions was chosen in such a way that the irradiating ions were stopped in the masking spheres and, apart from the edges, were able to fully shadow the FeRh film. The ions reached the film only in the open areas between the masking spheres. The calculated ion ranges for the uncovered sample, for the silica, and polystyrene masks were found to be 101.9, 204.6, and 344.0 nm, respectively. In Figure 3, the Ne⁺ ion distributions are shown for each case.

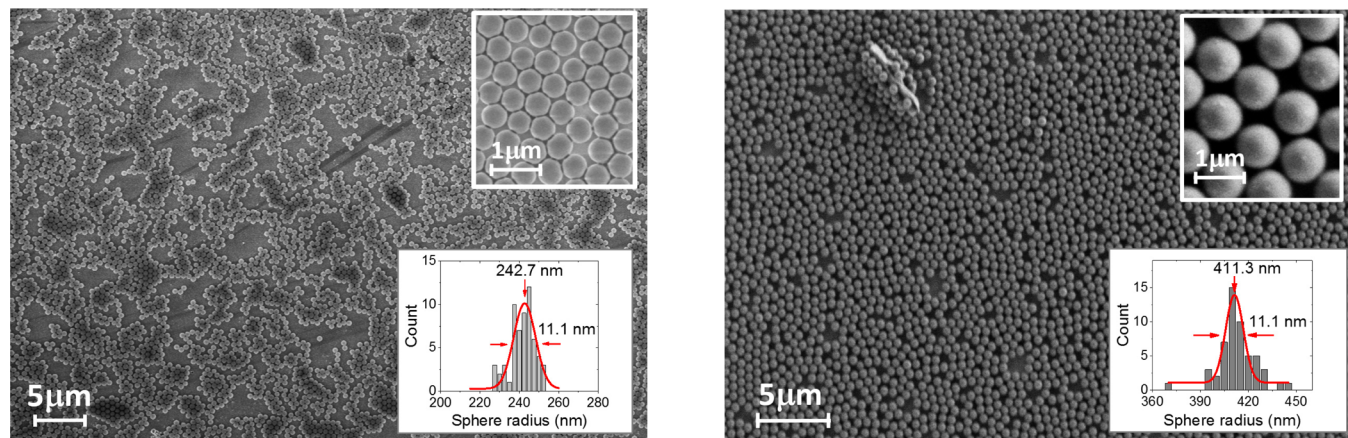


Figure 2. SEM images recorded from Langmuir–Blodgett monolayers of silica and polystyrene with different particle diameters. Image analysis revealed 485.4 and 822.6 nm median diameters for the respective spheres.

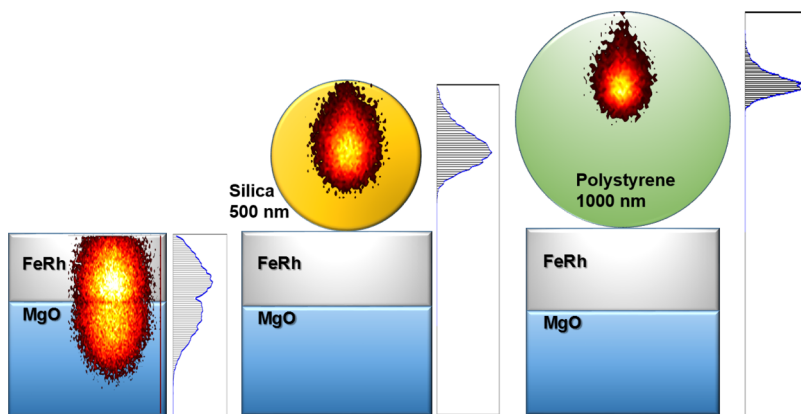


Figure 3. Simulated 110 keV Ne^+ ion distribution obtained after irradiation without mask (left), with a 500 nm silica (middle) and with a 1000 nm polystyrene shadow mask (right) on top of the sample.

After the irradiation, FESEM images were recorded again on the mask in order to investigate the damage and morphological change occurred in the nanoparticulate layer. Thereafter, the mask was removed from the sample using Scotch tape.

The obtained magnetic structure was investigated by MFM at room temperature. The MFM measurements were performed using a Bruker Icon MFM with PPP-MFMR cantilevers (NanosensorsTM). The standard dual-path mode was used, that is, the topography was acquired in a tapping mode, followed by the magnetic scan with the cantilever lift height of 60 nm. Gwyddion software was used to further analyze the recorded data.

CEMS experiments were done at room temperature using a conventional WissEl/DMSPCA Mössbauer spectrometer with a $^{57}\text{Co}(\text{Rh})$ source. Resonant conversion electrons were detected with a homemade gas-flow single-wire proportional counter working with a mixture of 96% He and 4% CH_4 gas. Throughout this study, values of the isomer shift are given with respect to $\alpha\text{-Fe}$ at room temperature. CEMS spectra were evaluated with the MossWinn 4.0 program.⁵⁹ Because thickness effects are negligible in the case of perpendicular-incidence CEMS,⁶⁰ Lorentzian line shapes of natural width were used for fitting the subspectra. To take into account the resonant self-absorption in the source and instrumental vibrations, the source spectrum was described by a pseudo-Voigt function, with the Lorentzian and Gaussian widths of 0.234 and 0.044 mm/s, respectively (values taken from the $\alpha\text{-}^{57}\text{Fe}$ calibration spectra), and the linewidths were fixed when fitting the CEMS spectra of the multilayers.

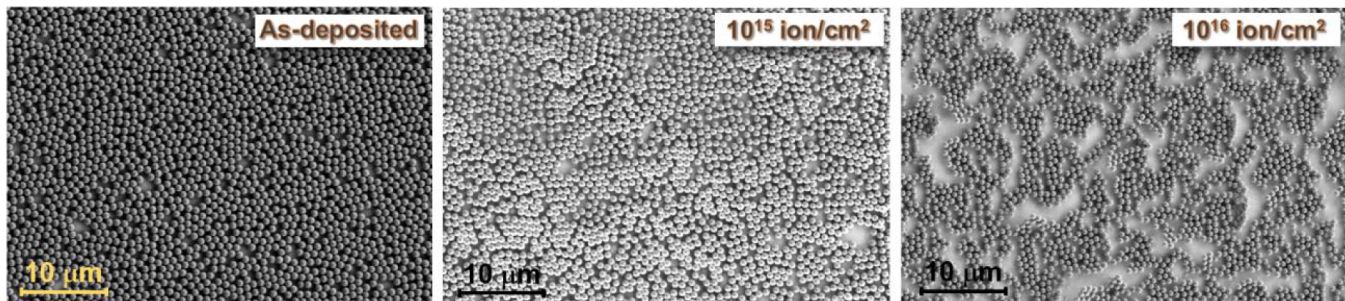
In addition, time-differential GINRS quantum-beat patterns and X-ray reflectivity (XRR) curves were recorded from each sample using a four-stack avalanche photodiode detector system with a time

resolution of ~ 1 ns. The experiment was carried out at the Nuclear Resonance beamline⁶¹ ID18 at ESRF in $(7/8 + 1)$ -bunch mode, using 14.41 keV beam energy, that is, the excitation energy of the ^{57}Fe nucleus. The source beam was provided by a high-resolution monochromator with 2 meV energy resolution. The beam was focused on the sample by Kirkpatrick–Baez (KB) mirrors reaching the beam size 3.2 μm horizontally and 4.2 μm vertically. Both GINRS and XRR data were evaluated by using the FitSuite program.⁶²

RESULTS AND DISCUSSION

In order to obtain the complete picture of the patterning process, one has to pay attention to how the spherical mask was influenced by the incoming Ne^+ ions. From the analysis of the FESEM images (Figure 4), we found a significant impact of the irradiation on the size of the polystyrene spheres. From the initial 411 nm radius (FWHM 11 nm), the sphere radius decreased to 382 nm (FWHM 23 nm) and 354 nm (FWHM 16 nm) in the case of the 10^{15} and 10^{16} ion/ cm^2 fluence irradiation, respectively (Figure 4). A similar phenomenon has been reported recently in a work by V. Lotito and co-workers where monolayers of closely packed polystyrene particles were irradiated with 1 MeV oxygen ions.⁶³ These authors observed the reduction of the size and also flattening of the polystyrene particles. Nevertheless, in accordance with other studies using Ar^+ and Xe^+ ion irradiation,^{64,65} our silica mask showed great resistance against irradiation, maintaining a constant sphere size with increasing ion fluence.

1000 nm diameter polystyrene mask



500 nm diameter silica mask

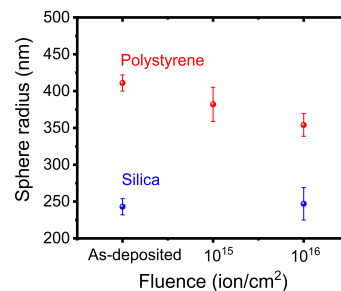
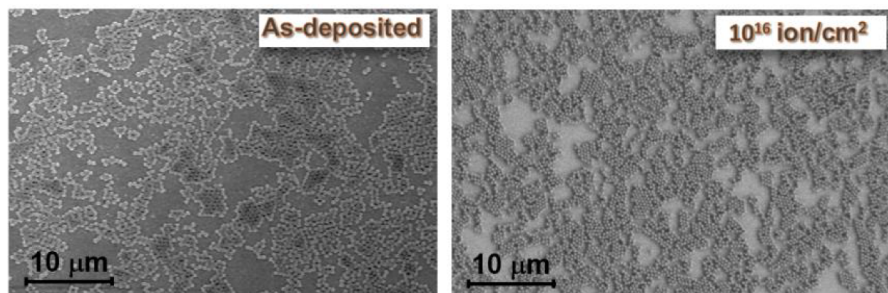


Figure 4. SEM images of silica and polystyrene masks recorded after deposition and after various dose irradiation with 110 keV Ne^+ ions and the change of the calculated sphere radius.

With the objective to follow the change in the ratio of magnetic and nonmagnetic components in the FeRh layer, CEMS measurements were carried out after each step of the experiment. Four main components, viz. two sextets, one singlet, and a doublet could be identified in a simultaneous fit of all spectra (**Figure 5**). The sextets, the singlet, and the doublet were assigned to the regular and antisite FM B2, the PM A1 phases, and the surface oxide,³⁹ respectively. The hyperfine parameters used for the evaluation are listed in **Table S1** in the Supporting Information.

The spectrum of the unirradiated sample exhibited 98.4% FM component, indicating full B2 ordering. Following the 110 keV Ne^+ irradiation, one could observe significant reduction of the FM concentration in the CEMS spectra, evidencing the B2 \rightarrow A1 (FM \rightarrow PM) transition. In the case of the 500 nm diameter nanosphere mask, the FM contribution was reduced to 22.7 and 6.0% after the neon fluence of 10^{15} and 10^{16} ion/cm^2 , respectively.

The same amount of irradiation had less impact in the case of the 1000 nm diameter nanosphere mask. After 10^{15} ion/cm^2 fluence irradiation, the FM component gave 52.5% contribution to the CEMS spectrum, and after the 10^{16} ion/cm^2 fluence irradiation, it decreased to 19.5%. The differences can be understood by looking at **Figure 2**, where the geometrical shadowing effect for the masks can be compared. The obtained relative areas for the individual subspectra for all samples are shown in **Table S2** in the Supporting Information. Because the CEMS measurements provide average information about the entire surface from about 50 nm depth,⁶⁰ it is not possible to locally describe the effect of masked irradiation. For this purpose, MFM images were also taken on each sample.

In **Figure 6**, the magnetic force microscopy images are shown in the unirradiated state and after 10^{15} and 10^{16} ion/cm^2

fluence Ne^+ irradiation. The unirradiated sample features a characteristic FM domain structure. With irradiation, we could observe the formation of FM regions in the PM matrix featuring the arrangement of the applied mask. In the case of the low fluence, the diameter of the FM regions was found to be smaller than the size of the mask. For silica mask, the average diameter obtained was 290(40) nm (484 nm mask size) and for the polystyrene mask, 810(70) nm (822 nm mask size). Increasing the fluence of irradiation, severe reduction in the domain size was observed. After 10^{16} ion/cm^2 Ne^+ irradiation, the average diameter of an FM region was found to be 220(30) and 520(50) nm for the silica and polystyrene mask, respectively.

By comparing the CEMS and MFM results, the ratios of FM/PM concentrations showed different values for the corresponding samples. In the case of MFM, the magnetic fractions were found to be systematically higher. This apparent contradiction may stem from the different analyzing depths of the various methods. While CEMS gives an average value from the entire volume of the sample from about 50 nm depth, MFM provides information about the projection of the magnetic geometry to the very near-surface region in the selected area. Therefore, if the size of the magnetic domains varies with depth in the film, the two techniques do not necessarily have to give the same result. In order to obtain direct evidence on the magnetic profile in the FeRh layer, GINRS experiments were carried out at three different scattering angles. The incident angles were selected so that the GINRS data carried information from different depth ranges of the film.^{66,67} The angles were chosen below, above, and exactly at the critical angle (0.236°) as it is marked on the reflectivity curve in **Figure 7a**. We performed simulations of the in-depth photon density at the selected angles (**Figure 7b,c**) for

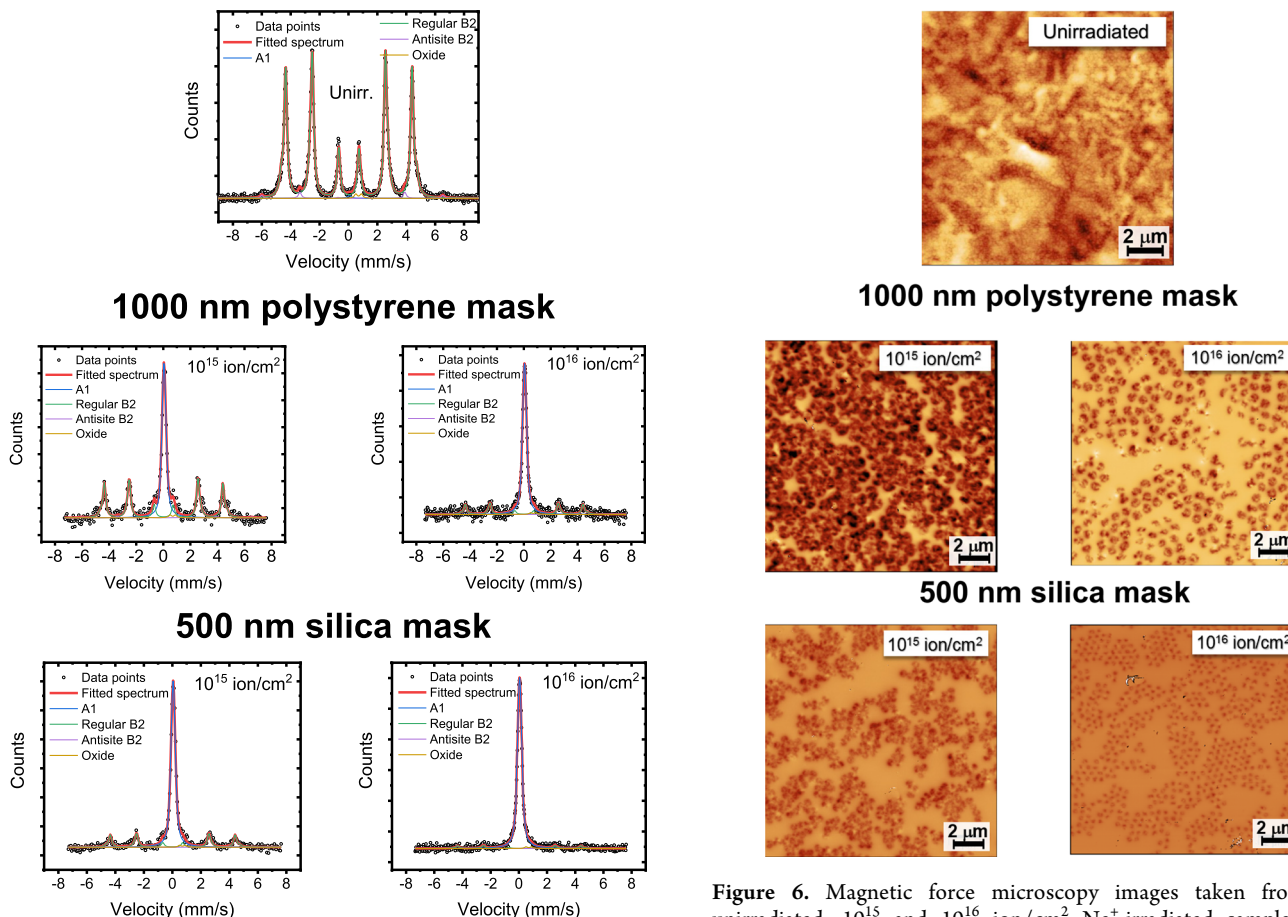


Figure 5. Conversion-electron Mössbauer spectra recorded on the unirradiated, 10^{15} and 10^{16} ion/cm² Ne^+ -irradiated samples with 500 nm silica and 1000 nm polystyrene.

fully FM and PM cases. The results clearly show how the photon penetration depth varies with the angle. It is apparent that at the resonance peaks, the penetration is quite shallow, but we have to keep in mind that in the measured quantum-beat patterns, the whole broadened lines play a role and not only their peaks. The information from the deep layers is provided by the contribution of the wavelengths at the sides of the broadened lines and not by the central ones that are absorbed strongly by the top layers. Applying the thickness data obtained from the evaluation of the reflectivity curve for the FeRh film thickness as well as the thickness of the formed oxide layer, the three GINRS spectra were evaluated simultaneously for each sample.

The hyperfine parameters were fixed at those obtained from CEMS data. The ratio of FM and PM components was individually assigned to each $^{57}\text{FeRh}$ layer in the sample, and the main fitting parameters were optimized to reconstruct all the measured data. Let us note that SRIM simulations indicate about 10 nm layer mixing (in the FWHM sense) between the substrate and the FeRh film for the uncovered part of the sample.

However, we could not see any difference in the magnetic behavior between the mixed and nonmixed regions; therefore, there is no significant effect on the formation of magnetic structures. The GINRS quantum-beat patterns recorded at three different grazing angles from unirradiated as well as the

polystyrene and silica-mask-covered Ne^+ -irradiated samples are shown in Figure 8.

The untreated sample features the high-frequency oscillation corresponding to almost the entire FM structure. In agreement with CEMS measurements, the irradiation induced the growth of the PM component at the expense of the FM phase, introducing low-frequency oscillations into the quantum-beat pattern. By comparing the corresponding GINRS quantum-beat patterns at different angles, it can be seen that the FM/PM ratio is highly sensitive to the angle of incidence, indicating the in-depth magnetic inhomogeneity in the samples.

From the evaluation of the GINRS data, the variation of the magnetic profiles in the FeRh layers vs depth was determined for each applied mask and used irradiation fluence. The obtained results, together with the corresponding CEMS and MFM values are shown in Figure 9a. In the case of the unirradiated sample, the FM concentration was basically constant (between 96 and 100%) throughout the film, showing discrepancies close to the substrate and air interfaces. The reduced FM/PM ratio at the FeRh/MgO interface may stem from the strained regions between the FeRh layer and the MgO substrate,⁶⁸ the coappearance of the B2 and A1 phases during the early stage of the deposition⁶⁹ and Fe- or Rh-rich regions.⁷⁰ The (slight) magnetic change in the FeRh/oxide interface can be explained by a local Rh surplus under the oxide layer, as a consequence of the iron-rich oxide layer on the top of the sample.⁷⁰ The common characteristics of each irradiated sample profile show a lower FM concentration

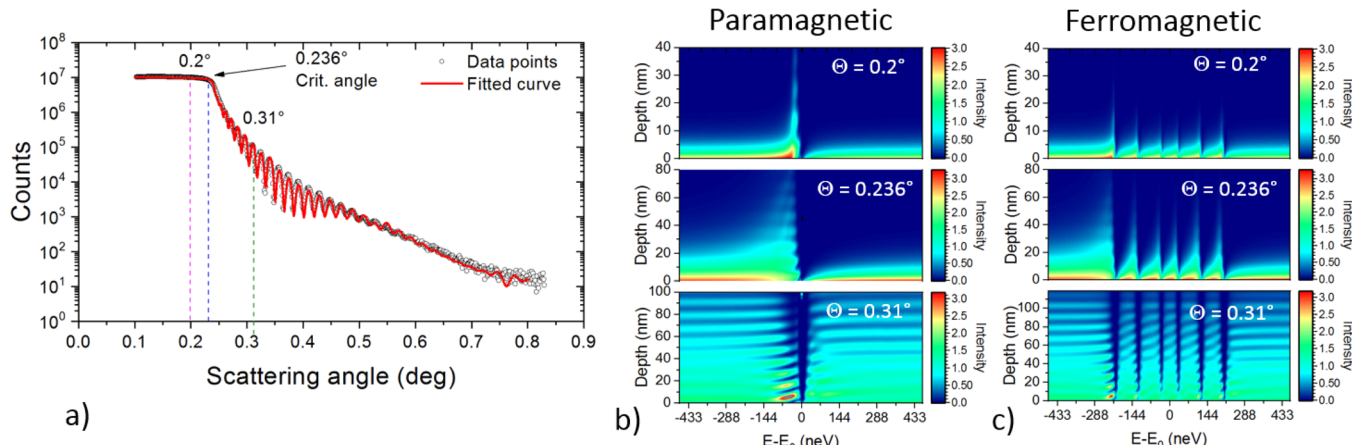


Figure 7. Nonresonant X-ray reflectivity curve of FeRh thin film. The dashed lines indicate the angles where the NRS patterns were recorded (a). In figure (b) and (c), the in-depth photon density (given in arbitrary units) of a fully PM (b) and fully FM (c) FeRh samples with the recent layer structure is shown as the function of energy detuning from the resonance at selected incident angles.

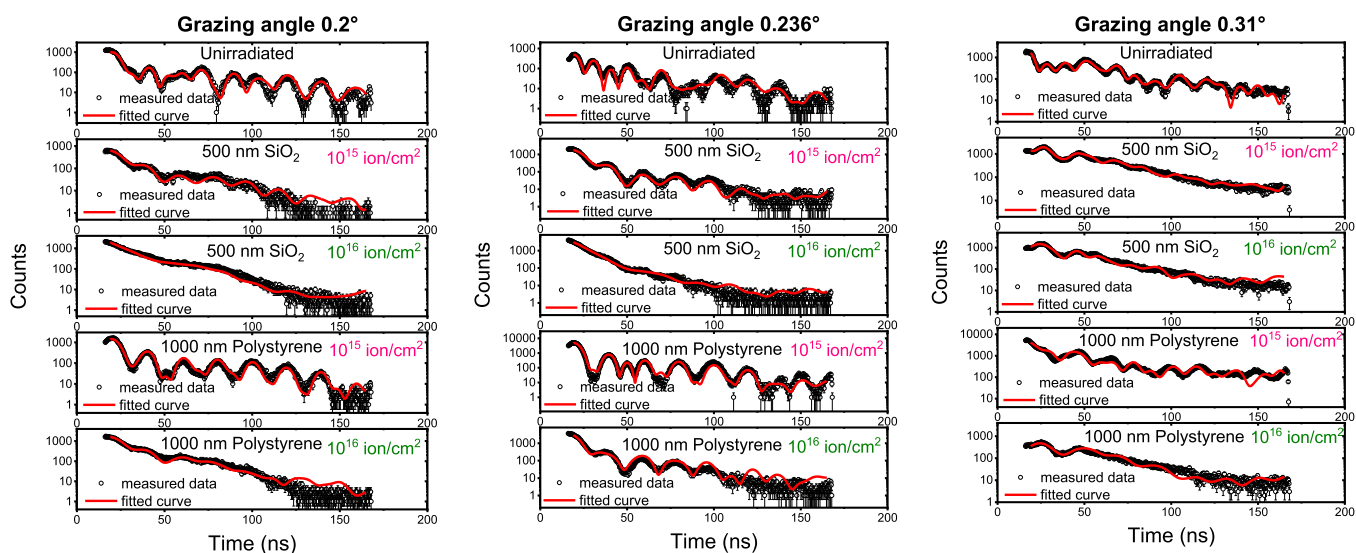


Figure 8. Grazing-incidence nuclear resonance scattering quantum-beat patterns recorded on the unirradiated, 10¹⁵ and 10¹⁶ ion/cm² irradiated samples with 500 nm silica and 1000 nm polystyrene applied masks.

directly below the upper interface, followed by a sudden increase in the FM ratio, and finally a slow decrease in the FM phase component. It should be noted that the MFM and GINRS techniques probe locally the sample (15 μm × 15 μm images for MFM and 3.2 μm wide stripe footprint for GINRS); therefore, the inhomogeneity in the coverage of the masking particles may lead to additional uncertainty of the FM/PM ratios compared to the ones obtained from image analysis or curve fitting.

We made an attempt to visualize the magnetic regions formed under the spherical mask based on the calculated magnetic profiles (Figure 9b). It was carried out using a standard 3D modeling software with no physical simulation option. By all means, the profiles cannot be transformed directly to 3D shapes, and, therefore, one has to introduce certain constraints. We assumed that, in accordance with the spherical shape of the masking particles, the formed magnetic domains will possess a rotational symmetry along the surface normal. Furthermore, the size distribution of the magnetic domains was not taken into account, and so the magnetic profiles give only an average value of the magnetic component

at a certain depth. It is also important that we cannot provide any information about the size of the domains, and only the FM/PM ratio of the sublayers relative to each other is known. The magnetic domains were built in a way that disk-shaped regions were assigned to sublayers, where the ratio of the area of each magnetic disk in the adjacent sublayers is exactly the same as we obtained from the FM/PM ratio of the GINRS experiment. We do not state that no other domain shape is possible, we only present a very likely formation, which is in full agreement with the measured data. By default, one would expect perfectly cylindrical-shaped magnetic domains in an idealized picture, where the spherical mask completely screens the irradiating ions moving parallel in the entire process. On the contrary, our results show an unusual magnetic domain profile as a consequence of several simultaneous effects, all of which influence the B2 → A1 transition at different depths. Because of the spherical shape of the mask, it is very important at which position the Ne⁺ ion passes through the mask. We performed calculations on the atomic displacement (DPA) induced by the irradiating ion in the FeRh film in the case where the Ne⁺ ion hits off-center the mask sphere (Figure

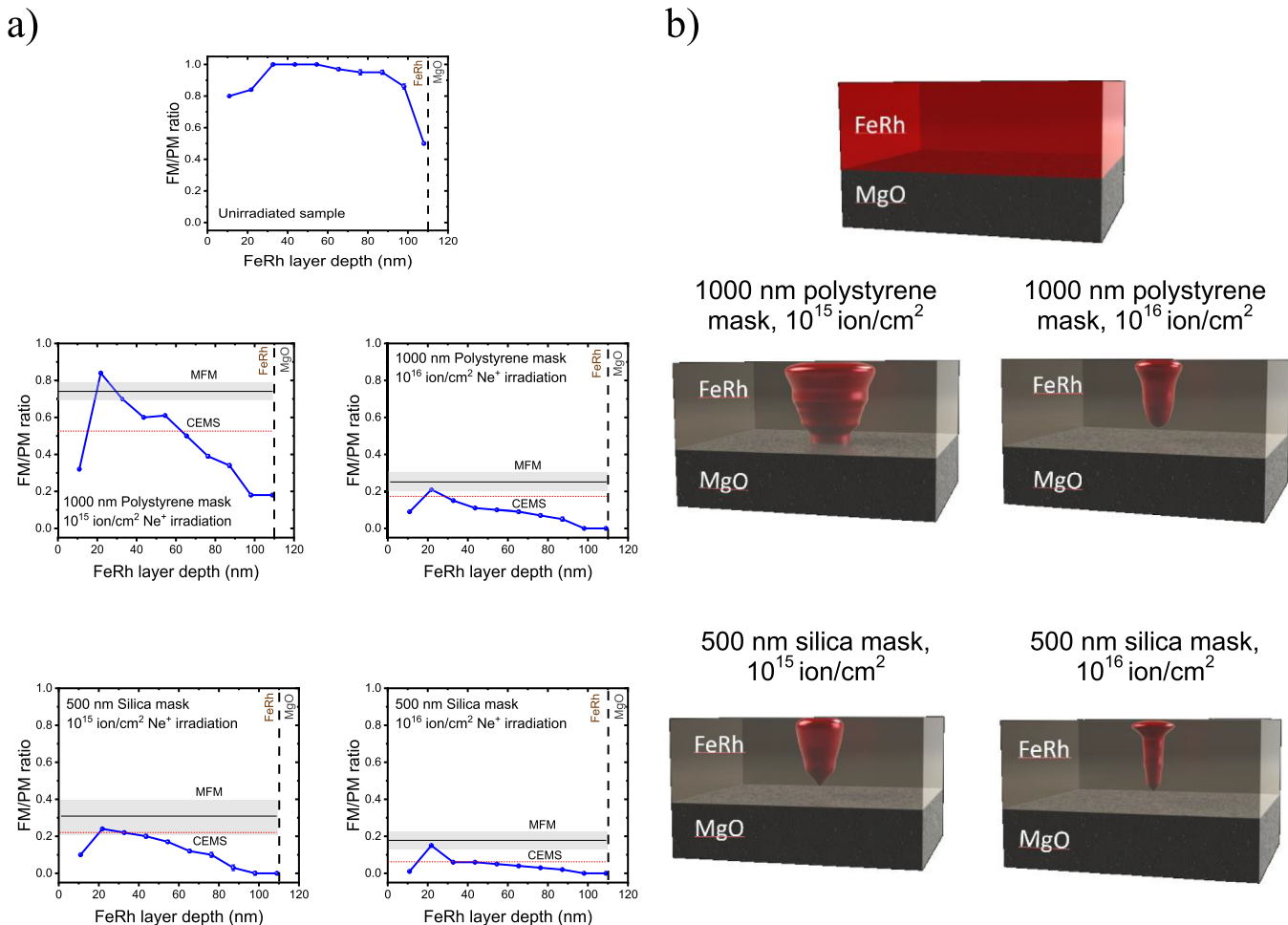


Figure 9. (a) Magnetic profiles of magnetic domains created after 10^{15} and 10^{16} ion/ cm^2 irradiation through 500 nm silica and 1000 nm polystyrene masks calculated from the evaluation of conversion-electron Mössbauer spectra and grazing-incidence nuclear resonance scattering quantum-beat patterns. (b) 3D representation of the magnetic domains in the FeRh film, where red color corresponds to the FM and brown to the PM magnetic ordering in the FeRh layer.

10b). It can be well seen that the majority of ions are absorbed by the mask, but some, after losing most of their energy, are able to reach the sample surface and turns FM regions to PM directly under the upper surface. It can be considered as low-energy irradiation, which is responsible for the narrowing of the upper part of the magnetic phase.

The continuous contraction of the magnetic area toward the bottom of the FeRh film most probably stems from the fact that the incoming ions do not pass through the layer in a straight line, but exhibit a lateral deviation. DPA calculations showed that this deviation increases with the penetration depth, and after a considerable lateral distance from the entry point of the ion, there are still significant collision events (Figure 10c) capable of inducing the $\text{B}2 \rightarrow \text{A}1$ transition. Moreover, if the irradiation ion hits the very edge of the sphere, the energy absorption can be neglected, but the ion undergoes “diffraction,” changing the incident angle and can directly go under the mask. In Figure 10d, the result of the SRIM simulation is shown concerning the Ne^+ -ion trajectory after passing through 50 Å silica, which represents the edge of the mask sphere. It can be clearly seen that a significant beam divergence appears, causing enhanced damage under the mask.

We think that the presented results can be directly utilized for engineering arbitrary FM regions in the PM matrix by

means of using custom irradiation mask. The discussion of the interaction of Ne^+ with FeRh film can also contribute to direct writing of FM areas with the help of focused ion-beam lithography. Moreover, it was shown that the variation of in-depth magnetism must be taken into account when a new device is developed based on this method.

CONCLUSIONS

Masked ion irradiation is an effective tool to create magnetic nanopatterns in FeRh thin films. Nanosphere masks were created on the top of FeRh films that were initially completely FM with a B2 structure. Silica and polystyrene spheres of 500 and 1000 nm in diameter, respectively, were used as masking particles. Then, the samples were irradiated by 110 keV Ne^+ ions with 10^{15} and 10^{16} ion/ cm^2 fluences in order to transform the unmasked areas of the film into an A1-structured PM substance while leaving the covered areas FM. The field emission electron microscopy technique was used to investigate the irradiation effect on the applied masks. Significant size degradation was observed in the case of polystyrene mask, while the silica mask remained intact.

By means of MFM and CEMS, we determined the change in FM and PM fractions because of the $\text{B}2 \rightarrow \text{A}1$ structural and magnetic transition. In order to determine the in-depth

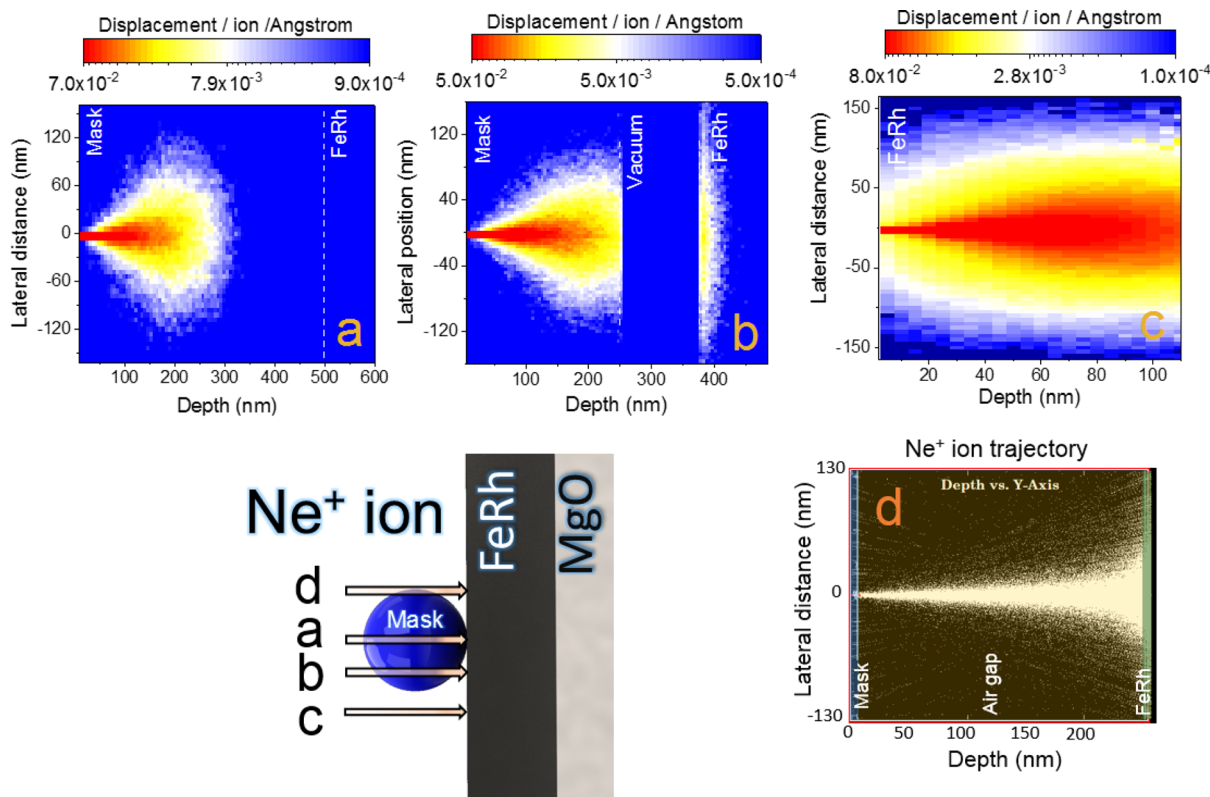


Figure 10. Calculated average number of displaced atoms (displacement/(Å ion)) caused by the irradiating Ne^+ ions at three different positions within the masking sphere ((a) at the sphere center, (b) at the side of the sphere, and (c) without mask). In the (d) figure, the Ne^+ -ion trajectory in the air gap between the mask and the sample surface is shown in case the Ne^+ ion hits the very edge of the sphere.

distribution of the magnetic structure, NRS experiments in the GI geometry were carried out. Based on the obtained lateral and in-depth magnetic profiles, the 3D interpretation of the magnetic domains for each type of mask geometry and irradiation fluence was provided.

By extending our results to custom-made mask lithography of focused ion-beam lithography, novel ways of fabricating modern FeRh-based magnetic nanodevices in the field of spintronics or information technology can be developed.

ASSOCIATED CONTENT

Supporting Information

The Supporting Information is available free of charge at <https://pubs.acs.org/doi/10.1021/acsanm.2c00511>.

Table of the hyperfine magnetic field (H), quadrupole splitting (ΔE), and isomer shift (δ) parameters of the different Fe environments in the FeRh sample. Table of the relative areas of all subspectra obtained from CEMS evaluation ([PDF](#))

AUTHOR INFORMATION

Corresponding Author

Dániel Géza Merkel – Institute for Particle and Nuclear Physics, Wigner Research Centre for Physics, Budapest 1121, Hungary; Neutron Spectroscopy Department, Centre for Energy Research, Budapest 1121, Hungary; [orcid.org/0000-0001-9644-2521](#); Email: merkel.daniel@wigner.hu

Authors

Gergő Hegedűs – Institute for Particle and Nuclear Physics, Wigner Research Centre for Physics, Budapest 1121, Hungary

Maria Gracheva – Institute of Chemistry, Eötvös Loránd University, Budapest 1117, Hungary; [orcid.org/0000-0001-5245-8425](#)

András Deák – Neutron Spectroscopy Department, Centre for Energy Research, Budapest 1121, Hungary

Levente Illés – Neutron Spectroscopy Department, Centre for Energy Research, Budapest 1121, Hungary

Attila Németh – Institute for Particle and Nuclear Physics, Wigner Research Centre for Physics, Budapest 1121, Hungary

Fernando Maccari – Functional Materials, Technische Universität Darmstadt, Darmstadt 64287, Germany

Iliya Radulov – Functional Materials, Technische Universität Darmstadt, Darmstadt 64287, Germany

Márton Major – Institute for Particle and Nuclear Physics, Wigner Research Centre for Physics, Budapest 1121, Hungary; Functional Materials, Technische Universität Darmstadt, Darmstadt 64287, Germany

Aleksandr I. Chumakov – ESRF-The European Synchrotron, Grenoble 38000, France; [orcid.org/0000-0002-0755-0422](#)

Dimitrios Bessas – ESRF-The European Synchrotron, Grenoble 38000, France

Dénes Lajos Nagy – Institute for Particle and Nuclear Physics, Wigner Research Centre for Physics, Budapest 1121, Hungary

Zsolt Zolnai – Neutron Spectroscopy Department, Centre for Energy Research, Budapest 1121, Hungary

Sára Graning – Institute of Physics, Budapest University of Technology and Economics, Budapest 1111, Hungary; Institute of Physics, Eötvös Loránd University, Budapest 1117, Hungary

Klára Sájerman – Institute of Physics, Budapest University of Technology and Economics, Budapest 1111, Hungary
Edit Szilágyi – Institute for Particle and Nuclear Physics, Wigner Research Centre for Physics, Budapest 1121, Hungary
Attila Lengyel – Institute for Particle and Nuclear Physics, Wigner Research Centre for Physics, Budapest 1121, Hungary

Complete contact information is available at:
<https://pubs.acs.org/10.1021/acsanm.2c00511>

Notes

The authors declare no competing financial interest.

ACKNOWLEDGMENTS

We acknowledge the European Synchrotron Radiation Facility for the provision of synchrotron radiation resources at the beamline ID18.

REFERENCES

- (1) Swartzendruber, L. J. The Fe–Rh (Iron-Rhodium) system. *Bull. Alloy Phase Diagrams* **1984**, *5*, 456–462.
- (2) Fina, I.; Dix, N.; Menéndez, E.; Crespi, A.; Foerster, M.; Aballe, L.; Sánchez, F.; Fontcuberta, J. Flexible Antiferromagnetic FeRh Tapes as Memory Elements. *ACS Appl. Mater. Interfaces* **2020**, *12*, 13.
- (3) Lee, Y.; Liu, Z. Q.; Heron, J. T.; Clarkson, J. D.; Hong, J.; Ko, C.; Biegalski, M. D.; Aschauer, U.; Hsu, S. L.; Nowakowski, M. E.; Wu, J.; Christen, H. M.; Salahuddin, S.; Bokor, J. B.; Spaldin, N. A.; Schlom, D. G.; Ramesh, R. Large resistivity modulation in mixed-phase metallic systems. *Nat. Commun.* **2015**, *6*, 5959.
- (4) Cress, C. D.; Wickramaratne, D.; Rosenberger, M. R.; Hennighausen, Z.; Callahan, P. G.; LaGasse, S. W.; Bernstein, N.; van't Erve, O. M.; Jonker, B. T.; Qadri, S. B.; Prestigiacomo, J. C.; Currie, M.; Mazin, I. I.; Bennett, S. P. Direct-Write of Nanoscale Domains with Tunable Metamagnetic Order in FeRh Thin Films. *ACS Appl. Mater. Interfaces* **2021**, *13*, 836–847.
- (5) Maruyama, T.; Shiota, Y.; Nozaki, T.; Ohta, K.; Toda, N.; Mizuguchi, M.; Tulapurkar, A. A.; Shinjo, T.; Shiraishi, M.; Mizukami, S.; Ando, Y.; Suzuki, Y. Large voltage-induced magnetic anisotropy change in a few atomic layers of iron. *Nat. Nanotechnol.* **2009**, *4*, 158–161.
- (6) Spaldin, N. A.; Cheong, S.; Ramesh, R. Multiferroics: Past, present, and future. *Phys. Today* **2010**, *63*, 38–43.
- (7) Heron, J. T.; Schlom, D. G.; Ramesh, R. Electric field control of magnetism using BiFeO₃-based heterostructures. *Appl. Phys. Rev.* **2014**, *1*, No. 021303.
- (8) Matsukura, F.; Tokura, Y.; Ohno, H. Control of magnetism by electric fields. *Nat. Nanotechnol.* **2015**, *10*, 209–220.
- (9) Fina, I.; Quintana, A.; Padilla-Pantoja, J.; Martí, X.; Macia, F.; Sanchez, F.; Foerster, M.; Aballe, L.; Fontcuberta, J.; Sort, J. Electric-Field-Adjustable Time-Dependent Magnetoelectric Response in Martensitic FeRh Alloy. *ACS Appl. Mater. Interfaces* **2017**, *9*, 15577–15582.
- (10) Nikitin, S.; Myalikgulyev, G.; Tishina, A. M.; Annaorazov, M. P.; Asatryan, K. A.; Tyurin, A. L. The magnetocaloric effect in Fe₄₉Rh₅₁ compound. *Phys. Lett. A* **1990**, *148*, 363–366.
- (11) Gutfleisch, O.; Gottschall, T.; Fries, M.; Benke, D.; Radulov, I.; Skokov, K. P.; Wende, H.; Gruner, M.; Acet, M.; Entel, P.; Farle, M. Mastering hysteresis in magnetocaloric materials. *Philos. Trans. R. Soc., A* **2016**, *374*, No. 20150308.
- (12) Gottschall, T.; Skokov, K. P.; Fries, M.; Taubel, A.; Radulov, I.; Scheibel, F.; Benke, D.; Riegg, S.; Gutfleisch, O. Making a Cool Choice: The Materials Library of Magnetic Refrigeration. *Adv. Energy Mater.* **2019**, *9*, No. 1901322.
- (13) Liu, Y.; Phillips, L.; Mattana, R.; Bibes, M.; Barthélémy, A.; Dkhil, B. Large reversible caloric effect in FeRh thin films via a dual-stimulus multicaloric cycle. *Nat. Commun.* **2016**, *7*, 1–6.
- (14) Tishin, A. M.; Spichkin, Y. I.; Zverev, V. I.; Egolf, P. W. A review and new perspectives for the magnetocaloric effect: new materials and local heating and cooling inside the human body. *Int. J. Refrig.* **2016**, *68*, 177–186.
- (15) Astefanoaei, I.; Dumitru, I.; Chiriac, H.; Stancu, A. L. Controlling temperature in magnetic hyperthermia with low Curie temperature particles. *J. Appl. Phys.* **2014**, *115*, 17B531.
- (16) Qiaoab, K.; Wangab, J.; Huab, F.; Li, J.; Zhang, C.; Liu, Y.; Yu, Z.; Gao, Y.; Su, J.; Shen, F.; Zhou, H.; Bai, X.; Wang, J.; Franco, V.; Sun, J.; Shen, B. Regulation of phase transition and magnetocaloric effect by ferroelectric domains in FeRh/PMN-PT heterojunctions. *Acta Mater.* **2020**, *191*, 51–59.
- (17) Chirkova, A.; Skokov, K. P.; Schultz, L.; Baranov, N. V.; Gutfleisch, O.; Woodcock, T. G. Giant adiabatic temperature change in FeRh alloys evidenced by direct measurements under cyclic conditions. *Acta Mater.* **2016**, *106*, 15–21.
- (18) Cherifi, R. O.; Ivanovskaya, V.; Phillips, L. C.; Zobelli, A.; Infante, I. C.; Jacquet, E.; Garcia, V.; Fusil, S.; Briddon, P. R.; Guiblin, N.; Mougin, A.; Ünal, A. A.; Kronast, F.; Valencia, S.; Dkhil, B.; Barthélémy, A.; Bibes, M. Electric-field control of magnetic order above room temperature. *Nat. Mater.* **2014**, *13*, 345–351.
- (19) Fina, I.; Quintana, A.; Martí, X.; Sánchez, F.; Foerster, M.; Aballe, L.; Sort, J.; Fontcuberta, J. Reversible and magnetically unassisted voltage-driven switching of magnetization in FeRh/PMN-PT. *Appl. Phys. Lett.* **2018**, *113*, 152901.
- (20) Muldawer, L.; de Bergevin, F. Antiferromagnetic-ferromagnetic transformation in FeRh. *J. Chem. Phys.* **1961**, *35*, 1904–1905.
- (21) Heeger, A. J. Pressure Dependence of the FeRh First-Order Phase Transition. *J. Appl. Phys.* **1970**, *41*, 4751–4752.
- (22) Schinkel, C. J.; Hartog, R.; Hochstenbach, F. H. A. M. On the magnetic and electrical properties of nearly equiatomic ordered FeRh alloys. *J. Phys. F: Met. Phys.* **1974**, *4*, 1412.
- (23) Amirov, A. A.; Rodionov, V. V.; Komanicky, V.; Latyshev, V.; Kanukov, E. Y.; Rodionova, V. V. Magnetic phase transition and magnetoelectric coupling in FeRh/PZT film composite. *J. Magn. Magn. Mater.* **2019**, *479*, 287–290.
- (24) Eggert, B.; Schmeink, A.; Lill, J.; Liedke, M. O.; Kentsch, U.; Butterling, M.; Wagner, A.; Pascarelli, S.; Potzger, K.; Lindner, J.; Thomson, T.; Fassbender, J.; Ollefs, K.; Keune, W.; Bali, R.; Wende, H. Magnetic response of FeRh to static and dynamic disorder. *RSC Adv.* **2020**, *10*, 14386–14395.
- (25) Shirane, G.; Chen, C. W.; Flinn, P. A.; Nathans, R. Hyperfine fields and magnetic moments in the Fe–Rh system. *J. Appl. Phys.* **1963**, *34*, 1044–1045.
- (26) Moruzzi, V. L.; Marcus, P. M. Antiferromagnetic-ferromagnetic transition in FeRh. *Phys. Rev. B* **1992**, *46*, 2864.
- (27) Arregi, J. A.; Horký, M.; Fabianová, K.; Tolley, R.; Fullerton, E. E.; Uhliř, V. Magnetization reversal and confinement effects across the metamagnetic phase transition in mesoscale FeRh structures. *J. Phys. D: Appl. Phys.* **2018**, *51*, 105001.
- (28) Lewis, L. H.; Marrows, C. H.; Langridge, S. Coupled magnetic, structural, and electronic phase transitions in FeRh. *J. Phys. D: Appl. Phys.* **2016**, *49*, No. 323002.
- (29) Phillips, L. C.; Cherifi, R. O.; Ivanovskaya, V.; Zobelli, A.; Infante, C.; Jacquet, E.; Guiblin, N.; Ünal, A. A.; Kronast, F.; Dkhil, B.; Barthélémy, A.; Bibes, M.; Valencia, S. Local electrical control of magnetic order and orientation by ferroelastic domain arrangements just above room temperature. *Sci. Rep.* **2015**, *5*, 1–8.
- (30) Witte, R.; Kruk, R.; Gruner, M. E.; Brand, R. A.; Wang, D.; Schlabauch, S.; Beck, A.; Provenzano, V.; Pentcheva, R.; Wende, H.; Hahn, H. Tailoring magnetic frustration in strained epitaxial FeRh films. *Phys. Rev. B* **2016**, *93*, No. 104416.
- (31) Witte, R.; Kruk, R.; Wang, D.; Schlabauch, S.; Brand, R. A.; Gruner, M. E.; Wende, H.; Hahn, H. Epitaxial strain adaptation in chemically disordered FeRh thin films. *Phys. Rev. B* **2019**, *99*, No. 134109.
- (32) Barton, C. W.; Ostler, T. A.; Huskisson, D.; Kinane, C. J.; Haigh, S. J.; Hrkac, G.; Thomson, T. Substrate induced strain field in FeRh epilayers grown on single crystal MgO (001) substrates. *Sci. Rep.* **2017**, *7*, 1–9.

- (33) Lu, W.; Huang, P.; Li, K.; Yan, B. Effect of substrate temperature on the crystallographic structure and first-order magnetic phase transition of FeRh thin films. *J. Mater. Res.* **2013**, *28*, 1042–1046.
- (34) Chao, C. C.; Duwez, P.; Tsuei, C. C. Metastable fcc Fe–Rh alloys and the Fe–Rh phase diagram. *J. Appl. Phys.* **1971**, *42*, 4282–4284.
- (35) Lommel, J. M.; Kouvel, J. S. Effects of mechanical and thermal treatment on the structure and magnetic transitions in FeRh. *J. Appl. Phys.* **1967**, *38*, 1263–1264.
- (36) Aikoh, K.; Kosugi, S.; Matsui, T.; Iwase, A. Quantitative control of magnetic ordering in FeRh thin films using 30 keV Ga ion irradiation from a focused ion beam system. *J. Appl. Phys.* **2011**, *109*, 07E311.
- (37) Fujita, N.; Kosugi, S.; Saitoh, Y.; Kaneta, Y.; Kume, K.; Batchuluun, T.; Ishikawa, N.; Matsui, T.; Iwase, A. Magnetic states controlled by energetic ion irradiation in FeRh thin films. *J. Appl. Phys.* **2010**, *107*, No. 09E302.
- (38) Heidarian, A.; Bali, R.; Grenzer, J.; Wilhelm, R. A.; Heller, R.; Yıldırım, O.; Lindner, J.; Potzger, K. Tuning the antiferromagnetic to ferromagnetic phase transition in FeRh thin films by means of low-energy/low fluence ion irradiation. *Nucl. Instrum. Methods Phys. Res., Sect. B* **2015**, *358*, 251–254.
- (39) Merkel, D. G.; Lengyel, A.; Nagy, D. L.; Németh, A.; Horváth, Z. E.; Bogdán, C.; Gracheva, M. A.; Hegedűs, G.; Sajti, S.; Radnóczí, G. Z.; Szilágyi, E. Reversible control of magnetism in FeRh thin films. *Sci. Rep.* **2020**, *10*, 1–11.
- (40) Kosugi, S.; Fujita, N.; Matsui, T.; Hori, F.; Saitoh, Y.; Ishikawa, N.; Okamoto, Y.; Iwase, A. Effect of high temperature annealing on ferromagnetism induced by energetic ion irradiation in FeRh alloy. *Nucl. Instrum. Methods Phys. Res., Sect. B* **2011**, *269*, 869–872.
- (41) Iwase, A.; Yoneda, K.; Ishigami, R.; Matsui, T. Restoration of ion beam irradiation induced metastable magnetic states and lattice structures of FeRh thin films by heat treatments at elevated temperatures. *J. Magn. Magn. Mater.* **2020**, *515*, No. 167286.
- (42) Bennett, S. P.; LaGasse, S. W.; Currie, M.; Van't Erve, O.; Prestigiacomo, J. C.; Cress, C. D.; Qadri, S. B. N⁺ Irradiation and Substrate-Induced Variability in the Metamagnetic Phase Transition of FeRh Films. *Coatings* **2021**, *11*, 661.
- (43) Bennett, S. P.; Herklotz, A.; Cress, C. D.; Ievlev, A.; Rouleau, C. M.; Mazin, L. V. Magnetic order multilayering in FeRh thin films by He-Ion irradiation. *Mater. Res. Lett.* **2018**, *6*, 106–112.
- (44) Griggs, W.; Eggert, B.; Liedke, M. O.; Butterling, M.; Wagner, A.; Kentsch, U.; Hirschmann, E.; Grimes, M.; Caruana, A. J.; Kinane, C.; Wende, H.; Bali, R.; Thomson, T. Depth selective magnetic phase coexistence in FeRh thin films. *APL Mater.* **2020**, *8*, 121103.
- (45) Jiang, M.; Chen, X. Z.; Zhou, X. J.; Cui, B.; Yan, H.; Wu, Q.; Pan, F.; Song, C. Electrochemical control of the phase transition of ultrathin FeRh films. *Appl. Phys. Lett.* **2016**, *108*, 202404.
- (46) Wang, L.-W.; Cheng, C.-F.; Liao, J.-W.; Wang, C.-Y.; Wang, D.-S.; Huang, K.-F.; Lin, T.-Y.; Ho, R.-M.; Chena, L.-J.; Lai, C. Thermal dewetting with a chemically heterogeneous nano-template for self-assembled L1₀ FePt nanoparticle arrays. *Nanoscale* **2016**, *8*, 3926–3935.
- (47) Bird, S. M.; Galloway, J. M.; Rawlings, A. E.; Bramble, J. P.; Staniland, S. S. Taking a hard line with biotemplating: cobalt-doped magnetite magnetic nanoparticle arrays. *Nanoscale* **2015**, *7*, 7340–7351.
- (48) Merkel, D. G.; Bessas, D.; Zolnai, Z.; Rüffer, R.; Chumakov, A. I.; Paddubrouskaya, H.; Van Haesendonck, C.; Nagy, N.; Tóth, A. L.; Deák, A. Evolution of magnetism on a curved nano-surface. *Nanoscale* **2015**, *7*, 12878–12887.
- (49) Merkel, D. G.; Bottyán, L.; Tanczikó, F.; Zolnai, Z.; Nagy, N.; Vértesy, G.; Waizinger, J.; Bommer, L. Magnetic patterning perpendicular anisotropy FePd alloy films by masked ion irradiation. *J. Appl. Phys.* **2011**, *109*, 124302.
- (50) Krupinski, M.; Bali, R.; Mitin, D.; Sobieszczyk, P.; Gregor-Pawlowski, J.; Zarzycki, A.; Böttger, R.; Albrecht, M.; Potzger, K.; Marszałek, M. Ion induced ferromagnetism combined with self-assembly for large area magnetic modulation of thin films. *Nanoscale* **2019**, *11*, 8930–8939.
- (51) Ehrler, J.; He, M.; Shugaev, M. V.; Polushkin, N. I.; Wintz, S.; Liersch, V.; Cornelius, S.; Hübner, R.; Potzger, K.; Lindner, J.; Fassbender, J.; Ünal, A. A.; Valencia, S.; Kronast, F.; Zhigilei, L. V.; Bali, R. Laser-Rewriteable Ferromagnetism at Thin-Film Surfaces. *ACS Appl. Mater. Interfaces* **2018**, *10*, 15232–15239.
- (52) Polushkin, N. I.; Oliveira, V.; Vilar, R.; He, M.; Shugaev, M. V.; Zhigilei, L. V. Phase-Change Magnetic Memory: Rewritable Ferromagnetism by Laser Quenching of Chemical Disorder in Fe₆₀Al₄₀ Alloy. *Phys Rev. Applied* **2018**, *10*, No. 024023.
- (53) Graus, P.; Möller, T. B.; Leiderer, P.; Boneberg, J.; Polushkin, N. I. Direct laser interference patterning of nonvolatile magnetic nanostructures in Fe₆₀Al₄₀ alloy via disorder-induced ferromagnetism. *Opto-Electron. Adv.* **2020**, *3*, No. 190027.
- (54) Foerster, M.; Menéndez, E.; Coy, E.; Quintana, A.; Gómez-Olivella, C.; Esqué de los Ojos, D.; Vallcorba, O.; Frontera, C.; Aballe, L.; Nogués; Sort, J. J.; Fina, I. Local manipulation of metamagnetism by strain nanopatterning. *Mater. Horiz.* **2020**, *7*, 2056–2062.
- (55) Zámbó, D.; Szekrényes, D. P.; Pothorszky, S.; Nagy, N.; Deák, A. SERS Activity of Reporter-Particle-Loaded Single Plasmonic Nanovoids. *J. Phys. Chem. C* **2018**, *122*, 23683–23690.
- (56) Chen, S.-L.; Yuan, G.; Hu, C.-T. Preparation and size determination of monodisperse silica microspheres for particle size certified reference materials. *Powder Technol.* **2011**, *207*, 232–237.
- (57) Nečas, D.; Klapetek, P. Gwyddion: an open-source software for SPM data analysis. *Open Phys.* **2012**, *10*, 181–188.
- (58) Ziegler, J. F.; Biersack, J. P.; Littmark, U. SRIM—The stopping and range of ions in matter (2010). *Nucl. Instrum. Methods Phys. Res., Sect. B* **2010**, *268*, 1818–1823.
- (59) Klencsár, Z.; Kuzmann, E.; Vértesy, A. User-friendly software for Mössbauer spectrum analysis. *J. Radioanal. Nucl. Chem.* **1996**, *210*, 105–118.
- (60) Sajti, S.; Tanczikó, F.; Deák, L.; Nagy, D. L.; Bottyán, L. Angular dependence, blackness and polarization effects in integral conversion electron Mössbauer spectroscopy. *Nucl. Instrum. Methods Phys. Res., Sect. B* **2015**, *342*, 62–69.
- (61) Rüffer, R.; Chumakov, A. I. Nuclear Resonance Beamline at ESRF. *Il Nuovo Cimento D* **1996**, *18*, 375–379.
- (62) Sajti, S.; Spiering, H. FitSuite program, <http://www.fs.kfki.hu>.
- (63) Lotito, V.; Karlušić, M.; Jakšić, M.; Luketić, K. T.; Müller, U.; Zambelli, T.; Fazinić, S. Shape deformation in ion beam irradiated colloidal monolayers: An AFM investigation. *Nanomaterials* **2020**, *10*, 453.
- (64) Lugomera, S.; Zolnai, Z.; Tóth, A. L.; Deák, A.; Nagy, N. Ar⁺ ion irradiation-induced reorganization of colloidal silica nanoparticles in Langmuir–Blodgett monolayers. *Thin Solid Films* **2015**, *574*, 136–145.
- (65) Zolnai, Z.; Nagy, N.; Deák, A.; Battistig, G.; Kótai, E. Three-dimensional view of the shape, size, and atomic composition of ordered nanostructures by Rutherford backscattering spectrometry. *Phys. Rev. B* **2011**, *83*, No. 233302.
- (66) Chumakov, A. I.; Niesen, L.; Nagy, D. L.; Alp, E. E. Nuclear resonant scattering of synchrotron radiation by multilayers structures. *Hyperfine Interact.* **1999**, *123*, 427–454.
- (67) Nagy, D. L.; Bottyán, L.; Deák, L.; Dekoster, J.; Langouche, G.; Semenov, V. G.; Spiering, H.; Szilágyi, E. Synchrotron Mössbauer reflectometry in Materials Science, *Mössbauer Spectroscopy in Materials Science*, Springer, Dordrecht, 1999, 323–336, DOI: [10.1007/978-94-011-4548-0_30](https://doi.org/10.1007/978-94-011-4548-0_30).
- (68) Gatel, C.; Warot-Fonrose, B.; Biziere, N.; Rodríguez, L. A.; Reyes, D.; Cours, R.; Castilla, M.; Casanove, M. J. Inhomogeneous spatial distribution of the magnetic transition in an iron-rhodium thin film. *Nat. Commun.* **2017**, *8*, 15703.
- (69) Fan, R.; Kinane, C. J.; Charlton, T. R.; Dorner, R.; Ali, M.; de Vries, M. A.; Brydson, R. M. D.; Marrows, C. H.; Hickey, B. J.; Arena, D. A.; Tanner, B. K.; Nisbet, G.; Langridge, S. Ferromagnetism at the interfaces of antiferromagnetic FeRh epilayers. *Phys. Rev. B* **2010**, *82*, No. 184418.

- (70) Baldasseroni, C.; Pálsson, G. K.; Bordel, C.; Valencia, S.; Unal, A. A.; Kronast, F.; Nemsak, S.; Fadley, C. S.; Borchers, J. A.; Maranville, B. B.; Hellman, F. Effect of capping material on interfacial ferromagnetism in FeRh thin films. *J. Appl. Phys.* **2014**, *115*, No. 043919.

□ Recommended by ACS

Magnetically Enhanced Thermoelectric Performance of $\text{Ti}_{0.75}\text{NiSb}+x \text{ mol \% Fe}$ ($x = 0\text{--}5$) Nanocomposites

Feng Luo, Zhigang Sun, *et al.*

OCTOBER 02, 2022

ACS APPLIED MATERIALS & INTERFACES

READ ↗

Effects of Crystalline Disorder on Interfacial and Magnetic Properties of Sputtered Topological Insulator/Ferromagnet Heterostructures

Nirjhar Bhattacharjee, Nian Xiang Sun, *et al.*

AUGUST 31, 2022

ACS APPLIED ELECTRONIC MATERIALS

READ ↗

Programmable Spin–Orbit Torque Multistate Memory and Spin Logic Cell

Yibo Fan, Yufeng Tian, *et al.*

MARCH 29, 2022

ACS NANO

READ ↗

High-Quality Ferromagnet Fe_3GeTe_2 for High-Efficiency Electromagnetic Wave Absorption and Shielding with Wideband Radar Cross Section Reduction

Guanghao Li, Yi Huang, *et al.*

APRIL 25, 2022

ACS NANO

READ ↗

[Get More Suggestions >](#)